Journal of Geophysical Research: Space Physics

RESEARCH ARTICLE
10.1029/2018JA025399

EISCAT Observation of Wave-Like Fluctuations in Vertical Velocity of Polar Mesospheric Summer Echoes Associated With a Geomagnetic Disturbance

Young-Sook Lee[1], Yong Ha Kim[1], Kyung-Chan Kim[2], Young-Sil Kwak[3,4], Timothy Sergienko[5], Sheila Kirkwood[5], and Magnar G. Johnsen[6]

[1]Department of Astronomy and Space Science, Chungnam National University, Daejeon, South Korea, [2]Division of Science Education, College of Education, Daegu University, Gyeongsan, South Korea, [3]Korea Astronomy and Space Science Institute, Daejeon, South Korea, [4]Department of Astronomy and Space Science, University of Science and Technology, Daejeon, South Korea, [5]Swedish Institute of Space Physics, Kiruna, Sweden, [6]Tromsø Geophysical Observatory, UiT-The Arctic University of Norway, Tromsø, Norway

Abstract By analyzing a data set from the European Incoherent SCATter (EISCAT) Very High Frequency (VHF) radar at Tromsø, we find that both radar reflectivity and upward ion velocity in a polar mesospheric summer echo (PMSE) layer simultaneously increased at the commencement of a local geomagnetic disturbance, which occurred at midnight on 9 July 2013. The onset of the upward velocity was followed by periodic repetition of ~5 min during the initial 30-min stage, and then at later stage the vertical velocity oscillated with ~7- and ~20-min periodicities at 85- to 90-km altitudes. The ~5-min periodicity is close to the buoyancy period, and the ~7- and ~20 min periodicities are consistent with gravity waves, thus suggesting that gravity waves can be generated by the effects of the geomagnetic disturbance. On the other hand, the variation of PMSE intensity (85–90 km) was in phase with fluctuations of electron densities (90–110 km) with ~12- and ~13-min periodicities at the initial and later stages, respectively. The initial creation of PMSE can be attributed to both the sudden onset of particle precipitation and ice particles produced by adiabatic cooling during the rapid updraft, as detected by large upward velocity. Our periodogram analysis suggests that variations of PMSE intensity seem to follow the same periods with *E* region electron density, which is moduled by energetic electron precipitation, while vertical velocity oscillates at atmospheric gravity wave periods.

Key Points:
- Vertical velocity of PMSE was observed to oscillate at near-buoyancy period of mesosphere after the onset of substorm
- Variation of PMSE intensity is well correlated with that of *E* region electron density
- Initial creation of PMSE is induced by both particle precipitation and air updraft that was observed as large upward velocity

Supporting Information:
- Supporting Information S1
- Figure S1

Correspondence to:
Y. H. Kim,
yhkim@cnu.ac.kr

Citation:
Lee, Y.-S., Kim, Y. H., Kim, K.-C., Kwak, Y.-S., Sergienko, T., Kirkwood, S., & Johnsen, M. G. (2018). EISCAT observation of wave-like fluctuations in vertical velocity of polar mesospheric summer echoes associated with a geomagnetic disturbance. *Journal of Geophysical Research: Space Physics*, *123*, 5182–5194. https://doi.org/10.1029/2018JA025399

Received 26 FEB 2018
Accepted 26 MAY 2018
Accepted article online 4 JUN 2018
Published online 15 JUN 2018

1. Introduction

Polar mesospheric summer echoes (PMSEs) are strong radar echoes reflected from fine structure in the electron gas surrounding charged subvisible ice particles. They have intrigued scientists since the first observation by Ecklund and Balsley (1981). When the particles grow larger, they are visible as noctilucent clouds or so-called polar mesospheric clouds (PMC). PMSE and PMC layers overlap in the lower part of 80- to 90-km altitudes, having drawn many attentions for the polar mesospheric study in summer. According to theory, PMSE can be detected due to complicated effects including influences of ice particles, electron density gradients, electron density enhancement, turbulence, and energetic electron precipitation during geomagnetic disturbance (Cho & Röttger, 1997; Varney et al., 2011).

Observational studies so far have not provided consistent pictures toward how PMSEs are related to radar echo's vertical velocity, turbulence, and geomagnetic disturbance. Effects of geomagnetic storms on PMSE were reported to be insignificant (in terms of *K* index; Bremer et al., 1995), while in later studies PMSE occurrence and its signal-to-noise ratio were well correlated with *K* and *AE* indices and with solar wind speed during high-speed solar wind streams (Lee et al., 2013; Zeller & Bremer, 2009). The upward (radial) velocity of radar echoes seems well correlated with enhanced PMSE power (higher signal-to-noise ratio; Bremer et al., 1995), while oscillation of the vertical velocity can sometimes lead that of PMSE power by 90° (Cho & Morley, 1995). In another case the upward velocity tends to make PMSE weaker (Hoppe & Fritts, 1995). Upward and downward velocities appear to be well correlated with upward and downward height transitions of PMSE (Fernandez et al., 2005), but in another study vertical velocities in a sinusoidal structure are 90° lagged behind PMSE altitudes in a wave-like structure (La Hoz et al., 1989). PMSEs are sometimes but not always associated with neutral turbulence since narrow spectral width of radar echoes (low turbulence) is frequently matched with PMSE occurrence (Strelnikova & Rapp, 2011; e.g., Lubken et al., 1993). These inconsistent observational results lead to a dilemma in explaining PMSE creation in connection to either

atmospheric-originated vertical velocity or geomagnetic disturbance (Cho & Röttger, 1997, and references therein). Although the source of PMSE's vertical velocity has been attributed to gravity wave propagation from the lower atmosphere (Fritts et al., 1988), it is so far unclear if enhanced vertical velocity might be linked to any other energy sources.

From the view point of geomagnetic disturbance, energetic particle precipitation has been identified as an important factor in producing PMSE, so that the energy source may not be limited to gravity wave-associated atmospheric dynamics (Lee et al., 2013, 2014). Periodic PMSEs (7- and 9-day periodicities) were observed to be correlated with recurrent high-speed solar wind streams during 2006 and 2008 summers (Lee et al., 2013). This correlation suggests that high-energy electron precipitation from the recurrent high-speed solar wind stream is the major contributor to PMSE occurrence. The periodic PMSEs were mostly led by peak occurrences of echo extreme horizontal drift speed (≥300 m/s), which were competitively affected by either solar wind dynamic pressure or high solar wind speed (Lee et al., 2014). In the meanwhile, short-period modulations (less than 30-min periodicity) of PMSE have not yet been comprehensively studied in respect of geomagnetic disturbance.

In this study utilizing the data set of PMSE and vertical ion velocity observed by the European Incoherent SCATter (EISCAT) VHF radar, we for the first time report the simultaneous increases of upward ion velocity and PMSE reflectivity driven by the sudden commencement of a geomagnetic disturbance. The simultaneous increase was followed by wave-like oscillations with various periods. In sections 2 and 3 the observed data set and characteristics of PMSE are described, respectively. In section 4, we examine whether the vertical velocity can be enhanced by geomagnetic disturbance, leading to gravity wave modulation. We probe the relationship between PMSE intensity and vertical velocity in section 5.1, and in section 5.2 we discuss whether short-period variations of PMSE are associated with modulated energetic electron precipitation or with gravity wave oscillations. The summary and conclusions are given in section 6.

2. Observations

For a case study on the northern summer mesospheric response to a geomagnetic disturbance, we selected a time period from 23 UT on 9 July to 1 UT on 10 July 2013, when the EISCAT VHF radar data are available for vertical velocity of ions and electron density/radar reflectivity in an altitude range of 70–120 km. The geomagnetic storm and substorms are identified with *Sym-H* and *AL*/*AU* indices and local magnetic field disturbance at Tromsø (69.6°N, 19.2°E), Norway, respectively.

The radar operated at a frequency of 224 MHz, on this occasion, as a monostatic system pointing to the vertical direction. In a *MANDA* mode the radar looks at relatively low altitudes of 50–180 km with height resolutions of 360 and 530 m at 80–95 km and 2–5 km at 95–120 km, with a time resolution of basically 6 s. For this study, the raw data are integrated by 1-min interval. Electron density is derived from the backscattered power detected at each height. The backscattered power is calibrated to provide a measurement of electron density at heights where incoherent scatter from thermal electrons dominates (in this case, above about 90-km altitude). Below 90-km altitude, coherent scatter from PMSE contributes to the backscattered signal so that a more appropriate measure of the received signal is radar reflectivity which is proportional to the *apparent electron density*. The GUISDAP software (Lehtinen & Huuskonen, 1996) returns a quantity of apparent electron density derived from the echo signal strength in assumption of a purely incoherent scatter mechanism. The provided electron density has been retrieved from volume reflectivity divided by the incoherent scatter cross section by GUISDAP algorithm. Hence, the reflectivity at PMSE altitudes is usually computed from the provided electron density using the linear relation of equation (1),

$$\eta = Ne \times \sigma, \tag{1}$$

where Ne is the provided electron number density (m^{-3}) and σ (=4.99×10^{-29} m^2) is the half of the Thomson scattering cross-section σ_e of an electron (i.e., $\sigma = \sigma_e \left(1 + \frac{T_e}{T_i}\right)^{-1} = \sigma_e/2$ for $T_e = T_i$, electron, and ion temperatures; e.g., Strelnikova & Rapp, 2011). For this analysis, equation (1) has been applied to all the electron density (80–120 km) provided by GUISDAP, so that the reflectivity at 80–90 km can represent that of PMSE, while the reflectivity above 90 km is meant to be proportional to the ionospheric electron density.

The vertical ion velocity is derived from the radial velocity deduced from the Doppler shift of ion motion, with the same method as used in Fritts et al. (1990). The allowed error is limited to 1 m/s. Due to the high ion-

neutral collision frequency in the mesosphere, the vertical ion velocity can be representative for the vertical velocity of neutral air below 90 km (Heelis, 2004). Data analysis in this study is primarily performed on both radar reflectivity and vertical velocity.

Geomagnetic field data at Tromsø are obtained from Tromsø Geophysical Observatory (http://flux.phys.uit.no/). Solar wind parameters are obtained from OMNIWeb which is hosted by NASA (http://omniweb.gsfc.nasa.gov). Precipitating high-energy electron fluxes (>30 and >100 keV) are obtained from the observation of the Medium Energy Proton and Electron Detector (MEPED) instrument in the Space Environment Monitor-2 experimental package onboard the National Oceanic and Atmospheric Administration-15, -16, and -18 Polar-orbiting Operational Environmental Satellites (POES).

3. Geomagnetic Disturbance and PMSE

In general, electron density in the *D* region ionosphere can be increased by the ionization induced by solar X-rays, by energetic electron precipitation, by solar proton events, by meteor shower, and by galactic cosmic ray (Aminaei et al., 2006; Chilton, 1961; Poppoff & Whitten, 1962; Velinov, 1968). We focus on the effect of high-energy electron precipitation on the observed radar reflectivity during a geomagnetic storm. For the chosen period, a shock-induced geomagnetic storm is identified from solar wind parameters and geomagnetic indices.

In Figure 1a, conditions of solar wind and geomagnetic activity are shown with the related parameters for the time period of day = 190–193.5 in 2013. Here solar wind parameters, geomagnetic disturbance index (*Sym-H*), auroral electrojet indices (*AL*/*AU*), *H* and *Z* components from the magnetometer at Tromsø are plotted at 1-min intervals in terms of universal time. For the corresponding period, (bottom panel) hourly variations of precipitating high-energy electrons for geomagnetic latitudes of 62–70°N (>30 keV [black], >100 keV [blue]) and hourly variations of reflectivity (η) of PMSE at 80–90 km (red) and reflectivity due to electron density at 100–120 km (orange) are plotted. Precipitating energetic electron fluxes were estimated by averaging MEPED data flux measured by POES-15, POES-16, and POES-18 at each hour for each energy channel. The solar wind shock can be noticed in the parameters of the solar wind dynamic pressure (Pdyn), the solar wind speed (Vsw), interplanetary magnetic field (IMF) *Bz*, and *Sym-H*, as indicated with the gray shaded region (Craven et al., 1986; Zhou & Tsurutani, 1999). On the shock arrival, the Pdyn is suddenly increased from 0.96 to 6 nPa for 19:40–21:35 on day = 190 (190.82–190.89), followed by an increase of solar wind speed, large fluctuations of IMF *Bz*, and a mild geomagnetic storm as indicated by *Sym-H*≈−50 nT. In addition, it is shown that the auroral electrojet indices *AL* (lower) and *AU* (upper) gradually increase after the Pdyn enhancement. As the *AL* index decreases, both PMSE reflectivity at 80–90 km and precipitating high-energy electron flux (>30 keV) are largely enhanced by 3 orders of magnitude from 10^{-18} to 10^{-15} m^{-1} and from 10^{2} to ~10^{5} $cm^{-3} \cdot s^{-1} \cdot sr^{-1}$, respectively. Reflectivity at 100–120 km is increased by as much as ~10 times due to electron density enhancement probably by auroral electron precipitation (<~30 keV). As well, the PMSE enhancement can be associated with *D* region ionization induced by high-energy electron precipitation (>30 keV; Kavanagh et al., 2012; Lee et al., 2013).

Magnetospheric ultra low frequency (ULF) pulsations in the frequency range of 1–100 mHz can be generated when ULF pulsations initiated around the bow shock region and magnetopause are crossing into the magnetosphere (O'Brien et al., 2003; Takahashi & Ukhorskiy, 2007; Waters et al., 2002, references therein). A fifth-order Butterworth band-pass filter with Pc5 frequency of 1.6–6.7 mHz is applied to Vsw, Pdyn, and the *H* component of the magnetic field and plotted in Figure 1b. Pc5 amplitudes of Vsw and Pdyn are enhanced after the shock arrival (indicated with vertical line A), and the amplitude of *H* oscillation in the Pc5 frequency band is enhanced after a negative excursion of the *H* component (vertical line B).

In order to examine how the radar reflectivity responds to the geomagnetic disturbance, we plot the altitude distribution of the radar reflectivity in Figure 2a. The radar reflectivity was linearly converted from the electron density that was measured by EISCAT as described in section 2. The red line in Figure 2a that indicates *H* component magnetogram measured at Tromsø is plotted with a range of ~$1.05 \times 10^{4} - 1.10 \times 10^{4}$ (nT; red ticks in left axis). From 116 km down to 70 km, the reflectivity becomes abruptly enhanced at 23:32 on day = 190, at the same time with a large drop of *H* component led by a small bump, which is a shock signature. Near this time, at 90–100 km a few spots of enhanced reflectivity are observed from an auroral sporadic *E* (metallic ion) layer, which is commonly embedded in EISCAT data (e.g., Kirkwood & Nilsson,

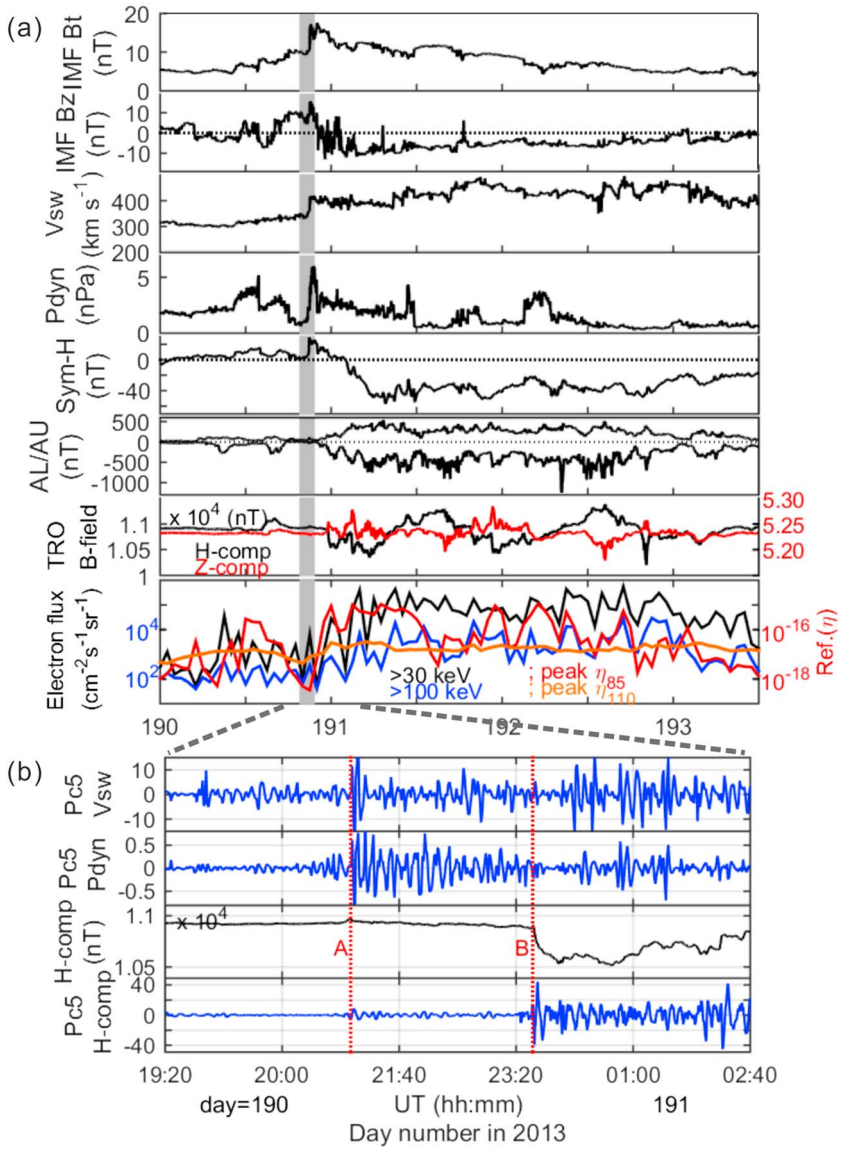

Figure 1. Solar wind shock (gray bar) and the subsequent geomagnetic storm and substorms, lasting for over 3 days: (a) From the top, solar wind parameters (1-min resolution) IMF magnitude (Bt), IMF *Bz* component (*Bz*), solar wind speed (Vsw), dynamic pressure (Pdyn), and geomagnetic storm index, *Sym-H*; auroral electrojet indices of *AL* (lower)/*AU* (upper) and geomagnetic fields of *H* (black) and *Z* (red) components at Tromsø; (bottom) hourly variations of electron >30-keV (black) and >100-keV fluxes (blue) and peak reflectivities (m^{-1}) at 80–90 km (η_{85}, red) and at 100–120 km (η_{110}, orange). (b) Detailed views of parameters for solar wind shock occurrence at A (red vertical dotted line) and the local geomagnetic disturbance at B (red vertical dotted line): (from the top) ULF Pc5 pulsations of Vsw and Pdyn and *H* component and *H*-Pc5 pulsation. Magnetic local time (MLT) at Tromsø is 2 hr ahead of UT (MLT = UT + 2). IMF = interplanetary magnetic field.

2000). At 80–90 km, two distinct strong echoes of wave-like structure can be recognized as PMSE. At the upper altitudes (85–90 km), PMSE appears to move up and down in altitude with a clustered manner, while at the lower altitudes (80–85 km) PMSE takes place in a narrower altitude region with much less intense reflectivity than those in 85–90 km. In Figure 2b, vertical velocities, for example, at 86.78 km representing for 85–90 km and at 83.18 km representing for 80–85 km are plotted from 23:00 UT, day = 190, to 01:00 UT, day = 191. At Tromsø, MLT = UT + 2 according to Altitude Adjusted Corrected Geomagnetic Coordinates model (Baker & Wing, 1989). Here for 86.78 km the upward velocity is largely enhanced up to ~12 m/s, caused by magnetic disturbances indicated with yellow bar and B, which is followed by frequent large upward velocities and later on by downward velocities (>±10 m/s). For

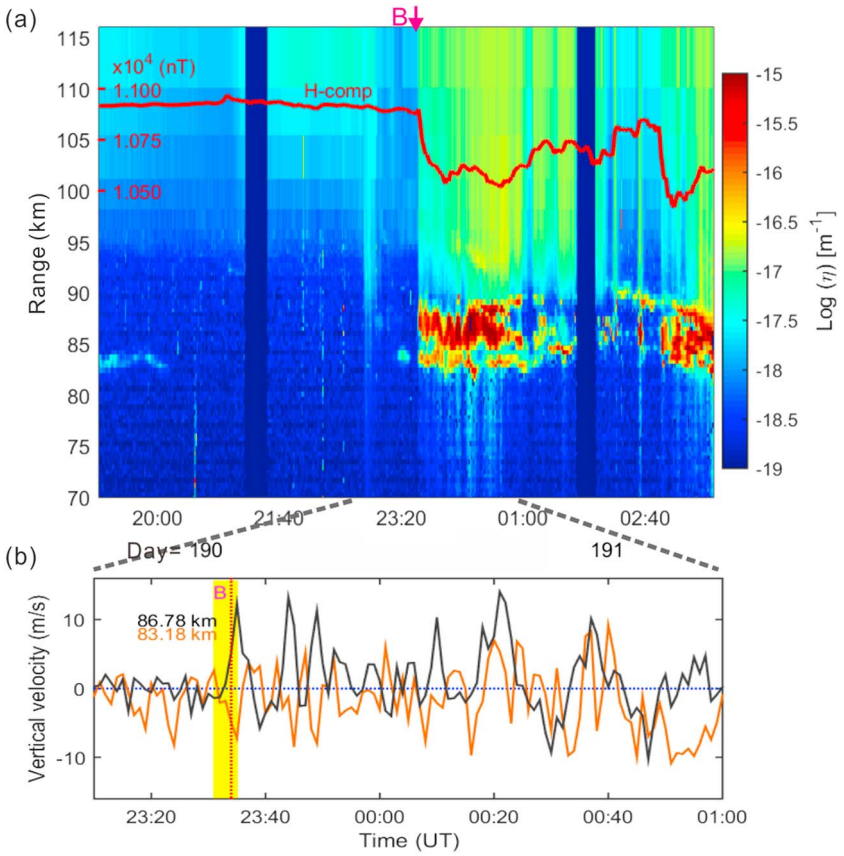

Figure 2. (a) Radar reflectivity as functions of time and altitude for a time interval from day = 190.80 (19:12 UT) to 191.15 (03:36 UT) measured by EISCAT radar, noted with color bar at the right side. Red line indicates *H* component at Tromsø, read with red tick labels in the left axis, and electron density (>90 km) breaks out according to the sudden drop of *H* component starting at 190.981 (23:32 UT). (b) Vertical velocity, for example, two selected range heights of 86.78 and 83.18 km for (upper) 85–90 km and (lower) 80–85 km, respectively. The time is elapsed from 00:00 UT, day = 190. EISCAT = European Incoherent SCATter; PMSE = polar mesospheric summer echo.

83.10 km, the upward velocity gradually increases after B event. The result implies that upward velocity above 85 km becomes more sensible to the magnetic field disturbance than below 85 km.

4. Reflectivity and Vertical Velocity Responses Under Geomagnetic Disturbance

In section 3, it is observed that as geomagnetic disturbance grows in response to the solar wind shock, PMSE reflectivity, electron density above 90 km, and upward velocity (80–90 km) are largely enhanced. For the detailed analysis, both reflectivity and vertical velocity presented in Figure 2 are averaged by a 5-km interval. For further analysis of reflectivity above 90 km, portions of sporadic *E* need to be removed. Sporadic *E* can be detected as scattered spikes or bumps (~2-km width) between 92 and 98 km (Kirkwood & Nilsson, 2000). In order to remove sporadic *E*, at first, mean value is derived from reflectivities at 92 ± 0.4 and 98 ± 0.4 km in min-to-min time variation, and then electron density bumps between 92 and 98 km are leveled down to the mean value at every minute.

Figure 3a shows detrended reflectivity (by removing low-frequency components <0.7 mHz or longer period of ~24 min) as functions of universal time. As shown in Figure 2a, the reflectivity of PMSE near B initially jumps up by as much as 3 orders of magnitude and then later on takes an additional increase by as much as 1 order of magnitude. By removing the low frequencies, the original magnitude is reduced but the short-period features are emphasized as in Figure 3a. A wave-like signature is distinctive at 85–90 km (gray shaded panel) where the echoes come from PMSE, and the wave signature is still evident with lower amplitudes at 70–80 km or 90–110 km where the echoes come from electron density. Note that the *y* axis range for the

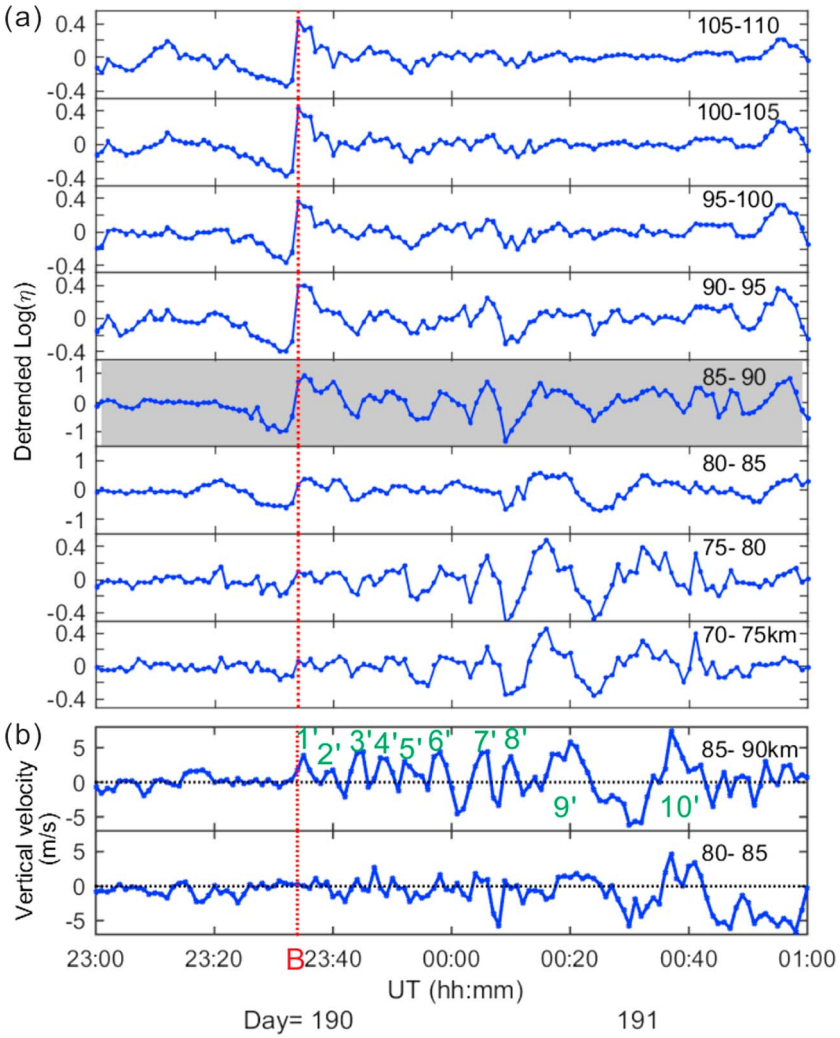

Figure 3. (a) Reflectivity after removing low-frequency part (<0.7 mHz), averaged at every 5 km interval from 70–110 km. (b) Vertical velocity averaged at 5 km from 80–90 km, except which range velocity is unavailable. Primed numbers of 1′–10′ indicate peaks of the velocity oscillations.

85- to 90-km panel is different for other panels. Below 80 km and above 90 km, it is well established that reflectivity enhancements (due to electron density increases) are readily induced by the energetic electron precipitation (Lee & Shepherd, 2007). As shown in Figure 1, high-energy electron precipitation is largely enhanced at the sudden negative excursion of geomagnetic field (*H* component). Electrons with energy (ε) higher than ~30 keV can reach effectively to altitudes of 80–90 km and those with ε>~100 keV to the lower altitudes (< 80 km). The large enhancements of cosmic noise absorption (due to an increase of *D* region electron density by energetic electron precipitation) have been reported in association with sudden storm commencement by Safargaleev et al. (2010). Thus, the wave-like structure above 90 km can be induced by the precipitation of energetic electrons modulated by whistler mode chorus waves which scatter electrons into the loss cone as they drift (Meredith et al., 2001).

The EISCAT radar beam was directed vertically in order to provide vertical ion velocity. In the overlapping region of the mesosphere and *D* region ionosphere, vertical ion velocity can be considered as vertical neutral velocity due to the high ion-neutral collisional frequency (Heelis, 2004). In Figure 3b, vertical velocities averaged with a 5-km interval are presented for 80–90 km. Note that there is no velocity available below 80 km or above 90 km since strong radar echoes from 80 to 90 km seem to contaminate the velocity measurement at other altitudes. According to Turunen et al. (2002), side lobe in the spatial ambiguity can reach the 1% of the main signal. This means that if in some altitude gate the back scattering power is more than 100 times higher

than in other gates, this huge signal will dominate in all gates in the altitude range corresponding to total pulse length of the radar. For the MANDA program this altitude range is equal to 43 km. Echo strengths in other gates are mostly less than 0.01 level of PMSE maximum. Here primed numbers of 1′–10′ indicate peaks of vertical velocity oscillations. It is noticeable that at the initial stage (from ~23:30 UT, day = 190) the vertical velocity at 85- to 90-km oscillates with a period of ~5 min for ~30 min (1′–6′). The oscillations (1′–5′) are dominated by upward velocity that reaches up to 5 m/s (or up to ~12 m/s, before being averaged over the 5-km interval as shown in Figure 2b). Downward velocity in the oscillation cycle is negligible, that is, upward biased, as was prior to the disturbance (marked with B line). After the initial stage, the period changed to ~7 min (7′–8′) and then 18–20 min (9′–10′).

The period of ~5 min at the initial stage is close to typical atmospheric buoyancy periods in the turbulent layer in the mesopause region (Dalin et al., 2012; Gibson-Wilde et al., 2000). Vertical velocity oscillations with a period of ~5 min suggest that gravity waves were generated by the initial rapid upward motion of air parcels at speeds $>$10 m/s (before averaged over 5-km altitude) and subsequently air parcels oscillated at the buoyancy frequency. It is remarkable that this gravity wave generation seems to occur directly in association with the geomagnetic disturbance driven by the solar wind shock and storm. The longer period of oscillation at the later stage may suggest a decrease in the vertical gradient of temperature since the buoyancy frequency depends on temperature and temperature gradient as shown in equation (2).

$$N(T,\ \mathrm{d}T/\mathrm{d}z) = \sqrt{\frac{g}{T}\left(\frac{\mathrm{d}T}{\mathrm{d}z} - \Gamma\right)} \tag{2}$$

where Γ is the dry adiabatic lapse rate (Andrews, 2000).

The upward biased oscillation at the initial stage can indicate an occurrence of neutral air lift. The updraft of air might be induced by a burst of heating in the atmosphere. The high energetic electron precipitation should first influence the neutral atmosphere (temperature, density, or composition) through Joule heating, particle heating, and chemical heating or other processes (see review by Sinnhuber et al., 2012). The oscillation at the initial stage also shows shorter periodicity (~5 min), while the oscillation at the later stage is not upward biased with the longer periodic oscillations (7 and 20 min). This may indicate that the oscillation at the initial stage be due to a gravity wave embedded in the updraft of heated air (upward bias) with low temperature gradient (shorter period), whereas those at the later stage be due to gravity waves in the cooled down atmosphere (no bias in vertical oscillation and longer periods). The mesospheric modulation by energetic electron precipitation has been found in recent observations by Hocke (2017), Yi, Reid, Xue, Younger, Spargo, et al. (2017), and Yi, Reid, Xue, Younger, Murphy, et al. (2017, references therein).

In the meanwhile, at 80–85 km, an increase of upward velocity seems delayed to cause oscillations (7′–10′) of vertical velocity. Therefore, at the later stage energetic particle precipitation must have reached down to 80 km and below as indicated in Figure 2a, thereby causing oscillation of neutral air parcels in the altitude range of 80–90 km. The delay of upward velocity increase may relent the doubts that gravity waves have existed since geomagnetically quiet time and manifested by the electron density increase. In this aspect, vertical velocity at the initial stage (23:30–23:50, day = 190) at 80–85 km is maintained at about the same level as before the onset in spite of enhancement of PMSE reflectivity at those altitudes and then later on represents increased magnitudes of periodic oscillation (likely gravity wave) after ~30 min passed from the onset.

5. Relationship Between PMSE and Vertical Velocity

In PMSE physics, PMSE creation is closely related to vertical motion, although with varying phase relationships (Bremer et al., 1995; Cho & Morley, 1995; Fernandez et al., 2005; Hoppe & Fritts, 1995). To determine whether or not vertical velocity has an effect on PMSE reflectivity increase, we examine their relationship first by comparing in time variation and second by Lomb-Scargle periodogram analysis.

5.1. Comparison in Time Variation

In this section, we compare behaviors of vertical velocity and PMSE with respect to universal time. In Figure 4, variations of vertical velocity and reflectivity at 80–90 km and the geomagnetic field are plotted as functions of time. At the start of the geomagnetic disturbance, electron precipitation is largely enhanced, as observed by MEPED onboard POES as shown in Figure 1 (e.g., Safargaleev et al., 2010). At the same time, vertical

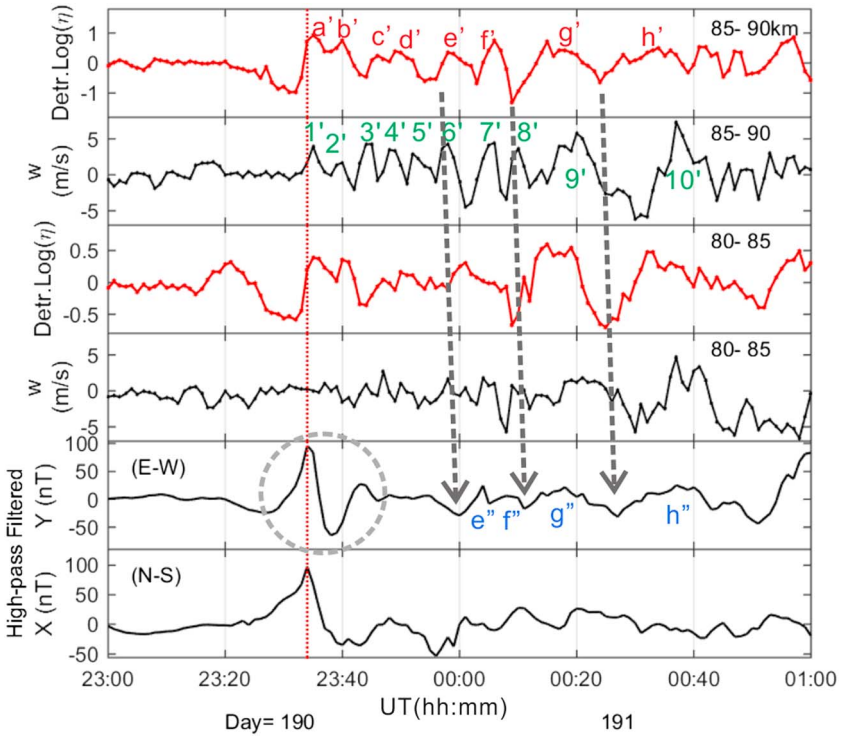

Figure 4. Comparison between reflectivity (red) and vertical velocity (black), which are averaged at every 5 km in 1-min time resolution, from the top for 85–90 km and then for 80–85 km. Magnetic fields of *X* and *Y* components (*X* = *H* cos (*D*), N-S; *Y* = *H* sin (*D*), E-W) at Tromsø, detrended after removing low-frequency components (<0.7 mHz). Primed letters of a′–h′ indicate peaks of reflectivity oscillations. Primed numbers of 1′–10′ indicate peaks of the velocity oscillations. Double primed letters of e″–h″ indicate peaks of *Y* component oscillations.

velocity 1′ peak and reflectivity a′ peak, as indicated in the top two panels, coincide with each other and match with the first pulses of geomagnetic fields of *X* = *H* cos (*D*; N-S direction) and *Y* = *H* sin (*D*; E-W direction), where *H* and *D* are the horizontal component and declination angle of the geomagnetic field, respectively. The impulses of geomagnetic fields in *X* and *Y* components exist in original data, which can be found in supporting information Figure S1, and thus are not an artifact by filtering process.

Enhanced high-energy electron precipitation leads to increases of electron density in the *D* and *E* region ionosphere. However, in the PMSE region at 80–90 km, radar reflectivities are much more strongly increased than above 90 km (see Figure 2), suggesting that the increase of PMSE detectability might depend also on an increase of ice particle number density (Varney et al., 2011). The observed reflectivity above 90 km virtually represents *E* region electron densities. It is interesting that both jumps of upward velocity and reflectivity occurred simultaneously with large pulsations of *X* and *Y* components at 23:34 UT, day = 190 (B). The Joule heating induced by energetic electron precipitation would be followed by adiabatic expansion and cooling that leads to ice particle formation by condensation, resulting in enhanced radar reflection (e.g., Varney et al., 2011; Williams et al., 1989). Heating at such low altitude would require precipitating electrons with energies 30–100 keV. Such particles not only cause particle heating but also increase Joule heating via enhanced conductivity due to the increased electron density at low altitudes (Sinnhuber et al., 2012). An example of this kind of behavior during pulsating aurora has been shown by Hosokawa and Ogawa (2010). The second possibility is that irregularities and plasma turbulence can produce an electron Pedersen current, resulting in Joule heating, in the presence of a strong electric field, although it is not clear if this can occur below 90 km (Blix et al., 1994; Buchert et al., 2008).

Williams et al. (1989) observed oscillations, in phase, between PMSE and upward velocity with 27-min periodicity. The in-phase oscillation does not agree with obvious expectations since it implies that the observed echoes correspond to the maximum rate of adiabatic cooling rather than the minimum temperature. However, upward velocity can contribute to PMSE increases by at least two processes: First, ice particles

can be produced by adiabatic cooling due to the upward expansion and second, turbulence can be induced by breaking of the gravity wave and then increase PMSE. There is also the complication that rapid formation of new ice particles may dry out the atmosphere so that no more can form and thus limit the PMSE increase to only the first part of the uplift interval.

Figure 4 shows that peak pairs of (c′, 3′) and (d′, 4′) are not synchronized, but reflectivity (c′ and d′) seems lagged behind the vertical velocity peaks (3′ and 4′). This is what would be expected if cooling by adiabatic expansion dominates. The peak pairs of (b′, 2′), (e′, 6′), and (f′, 7′) seem to be in phase, possibly due to a combination of adiabatic cooling and drying out of the air. In contrast, the upward velocity of 8′ matches with f′ trough of PMSE intensity. There is no obvious explanation for this, but cases where upward velocity tends to make PMSE weaker have also been reported by Hoppe and Fritts (1995). From the conflicting observations it can be argued that the creation of new ice particles from adiabatic cooling can be one (but not unique) process contributing to the PMSE variations. Heating by persistent high-energy electron precipitation may compete with adiabatic cooling induced by the upward motion of the air in varying the PMSE reflectivity.

At altitudes of 80–85 km (the lower part of the PMSE layer) from 23:30 to 00:10 UT, upward motion is suppressed compared to that of 85–90 km, as shown in the second and fourth panels of Figure 4. This lower layer of PMSE could be frozen in structures under fossil neutral turbulence (Rapp & Lübken, 2003, 2004). At 80–85 km PMC typically are found, as large-sized ice particles (~20 nm), so that the atmospheric mobility can be reduced by larger ice particles than those above 85 km.

As shown in the bottom panels of Figure 4, intense pulses of geomagnetic field components occur in the interval of 23:30–23:40 UT (day = 190) with a quasi-sinusoidal wave (gray circle) specifically for the *Y* component (nT, E-W direction), continued with less distinct undulations. It is noticeable that the *Y* component is lagged by ~2 min behind the PMSE oscillations in the troughs of pairs (e′, e″), (f′, f″), and (g′, g″) after 00:00 UT at day = 191, as marked with dashed arrows. PMSE oscillations of e′, f′, and g′ are well correlated with the reflectivity above 90 km that represents electron density changes due to modulated energetic electron precipitation (Figure 3). This observation is similar to that of Saito (1978) in which Ps6-type Pi3 pulsation has been reported elsewhere as the *D* component (E-W but the same as *Y* component) with 90° lag behind the electron precipitation. In another case, a pulsating *X* component lagged behind a cosmic noise absorption oscillation was observed by Manninen et al. (2002). Therefore, geomagnetic pulsations which lag behind that of reflectivity can be a signature for magnetic field pulsations induced by ionospheric conductivity modulation corresponding to the modulated energetic electron precipitation.

5.2. Comparison in Periodicities

Periodic analysis may provide clarification on whether PMSE oscillation is related to those of *E* region electron density (90–110 km) or vertical velocity. Figures 5a and 5b show periodic signatures of vertical velocity (black) and PMSE and *E* region electron density (red) as functions of frequency (mHz, bottom *x* axis) and periods (min, upper *x* axis) that were derived from Lomb-Scargle periodogram analysis for different altitudes. Note that the vertical velocity is only available for altitudes of 80–90 km. For an interval of 23:30–00:00 UT, day = 190, vertical velocity oscillates dominantly with a period of 4.8 min (3.5 mHz) at 85–90 km, and the significant oscillation of electron density and PMSE oscillations is at ~12-min (~1.3 mHz) periodicity. For 23:56–01:00 UT, the dominant periodicity of vertical velocity at 80–95 km is ~20 min (~0.8 mHz). It is noticeable that both electron density (reflectivity above 90 km and below 80 km) and PMSE (reflectivity in 80–90 km) have a common primary periodicity at ~12 min (1.3 mHz) in the time interval of 23:30–00:00 UT and then at ~18.5 min (0.8 mHz) and ~13.2 min (1.2 mHz) in 23:00–01:00 UT. At 85–90 km, there is a rather strong periodicity of 7.1 min occurring for PMSE as an approximate harmonics of the dominant 13.2-min period. The presence of harmonic frequency may suggest that precipitating electrons be accelerated by some kind of resonance mechanism in the magnetosphere. In the 23:00–00:00 interval, a periodicity at ~12 min of PMSE appears all in the reflectivity (representing electron density) above 90-km altitude but is not coherent with that (4.8 min) of vertical velocity. In the later stage, 00:00–01:00 UT at day = 191, PMSE periodicities at 13.2 min (and possible harmonics at 7.1 min) and 18.5 min are common to those of electron densities above 90 km, and interestingly, the 20-min periodicity of vertical velocity occurs close to the longer period of 18.5 min.

Although periodograms (Figure 5) do not clearly show a 4-min periodicity, at a time interval of 00:40–01:00 at day = 191, vertical velocity seems to oscillate with ~4-min period as shown in Figure 4. The 1- to 5-min

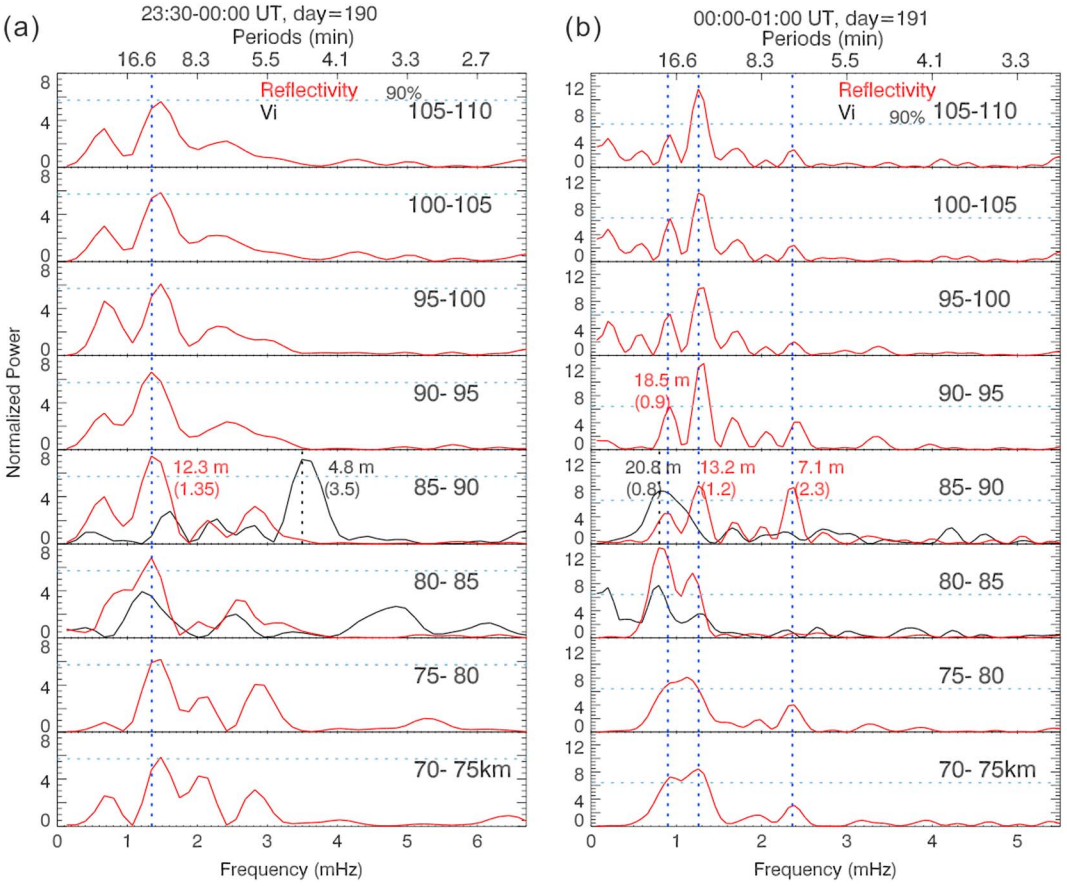

Figure 5. Lomb-Scargle periodigrams of reflectivity (red) and vertical velocity (black), which are averaged at every 5-km interval from 70 to 110 km for (a) 23:00–00:00 UT, day = 190–191, and (b) 00:00–01:00 UT, day = 191 (10 July 2013). *X* axis in the bottom for frequency (mHz) and in the top for period (min). Horizontal dotted line (blue) indicates 90% confidence level of the normalized power for both reflectivity and vertical velocity.

periods in the ionosphere can be identified with acoustic waves, which are usually detected above tropospheric convection (e.g., Blanc et al., 2010, references therein). Infrasonic waves are the source of acoustic waves, generated by severe weather, the solar eclipses, volcanic eruptions, and meteorites. In addition, auroral arcs moving in supersonic speed can generate auroral infrasonic wave, associated with energetic electron precipitation. The Joule heating of atmosphere and the Lorentz force mechanism can account for the generation of the auroral infrasonic waves (Wilson, 1969). The possibility of acoustic waves is congruous with observations of supersonic horizontal velocity in PMC/PMSE layers by Lee and Shepherd (2010) and Lee et al. (2014). Further investigation is, however, needed.

It is noticeable in that periodicities of 7–18.5 min in the PMSE reflectivity is aligned with the periodicities of *E* region electron density reflectivity. Electron density in the auroral latitude increase depends on the energetic electrons scattered from the magnetosphere. It is well established that ULF Pc5-Pc6 pulsations (0.7–6.7 mHz) can play an important role in modulating the growth rate of whistler mode chorus wave in the magnetosphere and consequently lead to periodic scattering of the accelerated electrons into the atmosphere (Coroniti & Kennell, 1970; Li et al., 2009; O'Brien et al., 2003). Zolotukhina et al. (2008) observed Pc5 wave generation in the geomagnetic field disturbance ~10 min after substorm onset in the magnetosphere by the Geostationary Operational Environmental Satellite Program satellite measurements. Overall results from our period analysis suggest that initial PMSE can be largely enhanced both by outburst of energetic electron precipitation and adiabatic cooling caused by initially large upward velocity. Variations of PMSE intensity, however, seem tied to the oscillation of *E* region electron densities, which is in turn linked to modulated energetic electron precipitation from the magnetosphere, whereas the vertical velocities of the air may oscillate with the gravity waves that were generated initially by the large updraft at the onset of substorm.

6. Summary and Conclusions

From radar reflectivity and vertical velocity measured by EISCAT VHF radar, simultaneous onsets of PMSE and large upward velocity (80–90 km), along with enhanced *E* region electron density (90–110 km), are found at the time of a large negative excursion of the geomagnetic field at Tromsø. The onsets are followed by wave-like structures with a variety of periodicities. The analysis results are summarized as follows:

1. Upon the onset of the geomagnetic disturbance, a large upward velocity is observed, repeated at ~5-min interval at the initial stage for 30 min. The large upward repeated motion, or upward biased oscillation, implies a large updraft of the air heated by energetic electron precipitation accompanied by geomagnetic storm. The ~5-min upward biased oscillation can be a signature of gravity waves embedded in the updraft atmosphere heated by the geomagnetic disturbances.
2. The oscillation of vertical velocity at the later stage shows no upward bias and longer periods of ~7 and ~20 min. The oscillation may be indicative of gravity waves in the cooled down atmosphere which is at rest vertically.
3. At the initial stage PMSE reflectivity shows oscillations of a 12.3-min periodicity for ~30 min. The oscillation continues with a primary (~13 min) and secondary (~18 min) periodicities for about an hour. The periodic oscillations of PMSE are mostly coincident, both in period and phase, with those of electron density-scattered reflectivities at 90- to 110-km heights. It seems likely that PMSE periodicities are associated with modulated electron precipitation.
4. The sudden enhancement of PMSE at the initial stage may be due to both enhanced energetic electron precipitation and adiabatic expansion by air updraft as detected with large upward velocity. The subsequent PMSE variations are associated with complicated modulations of the heating rate in the mesosphere, which seems to be mainly controlled by precipitating energetic electrons.

Acknowledgments
This study was funded by the KMA/NMSC (Korea Meteorological Administration/National Meteorological Satellite Center)'s R&D Project (NMSC-2016-3137). We thank EISCAT for the provision of VHF radar data and Tromsø Geophysical Observatory, UiT-The Arctic University of Norway, for providing the Tromsø magnetometer data. We also thank GSFC/SPDF OMNIWeb for the provision of the solar wind parameters and geomagnetic activity indices used in this study. The authors also express their appreciation of the National Centre for Environmental Information of the National Oceanic and Atmospheric Administration (NOAA) for the permission to use the MEPED data on the POES, which was downloaded from http://satdat.ngdc.noaa.gov/sem/poes/.

References

Aminaei, A., Honary, F., Kavanagh, A. J., Spanswick, E., & Viljanen, A. (2006). Characteristics of night-time absorption spike events. *Annales Geophysique*, *24*(7), 1887–1904. https://doi.org/10.5194/angeo-24-1887-2006

Andrews, D. G. (2000). *An introduction to atmospheric physics*. Cambridge, UK: Cambridge University Press. https://doi.org/10.1017/CBO9780511800771

Baker, K. B., & Wing, S. (1989). A new magnetic coordinate system for conjugate studies at high latitudes. *Journal of Geophysical Research*, *94*(A7), 9139–9143. https://doi.org/10.1029/JA094iA07p09139

Blanc, E., Le Pichon, A., Ceranna, L., Farges, T., Marty, J., & Herry, P. (2010). Global scale monitoring of acoustic and gravity waves for the study of the atmospheric dynamics. In A. Le Pichon, et al. (Eds.), *Infrasound monitoring for atmospheric studies* (pp. 647–664). Dordrecht: Springer. https://doi.org/10.1007/978-1-4020-9508-5_21

Blix, T. A., Thrane, E. V., Kirkwood, S., & Schlegel, K. (1994). Plasma instabilities in the lower E-region observed during the DYANA campaign. *Journal of Atmospheric and Terrestrial Physics*, *56*, 1853–1870.

Bremer, J., Singer, W., Keuer, D., Hoffmann, P., Rottger, J., Cho, J. Y. N., & Swartz, W. E. (1995). Observations of polar mesosphere summer echoes at EISCAT during summer 1991. *Radio Science*, *30*(4), 1219–1228. https://doi.org/10.1029/95RS00651

Buchert, S. C., Tsuda, T., Fujii, R., & Nozawa, S. (2008). The Pedersen current carried by electrons: A non-linear response of the ionosphere to magnetospheric forcing. *Annales Geophysique*, *26*, 2837–2844.

Chilton, C. J. (1961). VLF phase perturbation associated with meteor shower ionization. *Journal of Geophysical Research*, *66*(2), 379–383. https://doi.org/10.1029/JZ066i002p00379

Cho, J. Y. N., & Morley, R. L. (1995). PMSE dependence on long-period vertical motions. *Geophysical Research Letters*, *22*, 1197–1200. https://doi.org/10.1029/95GL01010

Cho, J. Y. N., & Röttger, J. (1997). An updated review of polar mesosphere summer echoes: Observation, theory, and their relationship to noctilucent clouds and subvisible aerosols. *Journal of Geophysical Research*, *102*(D2), 2001–2020. https://doi.org/10.1029/96JD02030

Coroniti, F. V., & Kennell, C. F. (1970). Electron precipitation pulsations. *Journal of Geophysical Research*, *75*, 1279–1289.

Craven, J. D., Frank, L. A., Russell, C. T., Smith, E. J., & Lepping, R. P. (1986). Global auroral responses to magnetospheric compressions by shocks in the solar wind: Two case studies. In Y. Kamide, & J. A. Slavin (Eds.), *Solar wind-magnetosphere coupling* (pp. 367–380). Tokyo, Japan: Terra Scientific Publishing Co.

Dalin, P., Kirkwood, S., Hervig, M., Mihalikova, M., Mikhaylova, D., Wolf, I., & Osepian, A. (2012). Wave influence on polar mesosphere summer echoes above Wasa: Experimental and model studies. *Annales Geophysique*, *30*, 1143–1157.

Ecklund, W. L., & Balsley, B. B. (1981). Long-term observations of the arctic mesosphere with the MST radar at Poker Flat, Alaska. *Journal of Geophysical Research*, *86*, 7775–7780. https://doi.org/10.1029/JA086iA09p07775

Fernandez, J. R., Palmer, R. D., Chilson, P. B., Haggstrom, I., & Rietveld, M. T. (2005). Range imaging observations of PMSE using the EISCAT VHF radar: Phase calibration and first results. *Annales Geophysique*, *23*, 207–220.

Fritts, D. C., Hppe, U.-P., & Inhester, B. (1990). A study of the vertical motion field near the high-latitude summer mesopause during MAC/SINE. *Journal of Atmospheric and Terrestrial Physics*, *52*, 927–938.

Fritts, D. C., Smith, S. A., Balsley, B. B., & Philbrick, C. R. (1988). Evidence of gravity wave saturation and local turbulence production in the summer mesosphere and lower thermosphere during the STATE experiment. *Journal of Geophysical Research*, *93*, 7015–7025.

Gibson-Wilde, D. E., Werne, J. A., Fritts, D. C., & Hill, R. J. (2000). Direct numerical simulation of VHF radar measurements of turbulence in the mesosphere. *Radio Science*, *35*, 783–798. https://doi.org/10.1029/1999RS002269

Heelis, R. A. (2004). Electrodynamics in the low and middle latitude ionosphere: A tutorial. *Journal of Atmospheric and Solar: Terrestrial Physics*, *66*, 825–838.
Hocke, K. (2017). Response of the middle atmosphere to the geomagnetic storm of November 2004. *Journal of Atmospheric and Solar: Terrestrial Physics*, *154*, 86–91. https://doi.org/10.1016/j.jastp.2016.12.013
Hoppe, U.-P., & Fritts, D. C. (1995). On the downward bias in vertical velocity measurements by VHF radars. *Geophysical Research Letters*, *22*(5), 619–622.
Hosokawa, K., & Ogawa, Y. (2010). Pedersen current carried by electrons in auroral D-region. *Geophysical Research Letters*, *37*, L18103. https://doi.org/10.1029/2010GL044746
Kavanagh, A. J., Honary, F., Donovan, E. F., Ulich, T., & Denton, M. H. (2012). Key features of >30 keV electron precipitation during high speed solar wind streams: A superposed epoch analysis. *Journal of Geophysical Research*, *117*, A00L09. https://doi.org/10.1029/2011JA017320
Kirkwood, S., & Nilsson, H. (2000). High-latitude sporadic-E and other thin layers—The role of magnetospheric electric fields. *Space Science Reviews*, *91*(3–4), 579–613.
La Hoz, C., J. Röttger & S.J. Franke (1989), Dynamic spectra of PMSE measured by EISCAT at 224 MHz, Handbook for MAP 28, 248-256.
Lee, Y.-S., Kirkwood, S., Kwak, Y.-S., Kim, K.-C., & Shepherd, G. G. (2014). Polar summer mesospheric extreme horizontal drift speeds during interplanetary corotating interaction regions (CIRs) and high-speed solar wind streams: Coupling between the solar wind and the mesosphere. *Journal of Geophysical Research: Space Physics*, *119*, 3883–3894. https://doi.org/10.1002/2014JA019790
Lee, Y.-S., Kirkwood, S., Shepherd, G. G., Kwak, Y.-S., & Kim, K.-C. (2013). Long-periodic strong radar echoes in the summer polar D region correlated with oscillations of high-speed solar wind streams. *Geophysical Research Letters*, *40*, 4160–4164. https://doi.org/10.1002/grl.50821
Lee, Y.-S., & Shepherd, G. G. (2007). Statistical comparison of WINDII auroral green line emission rate with DMSP/SSJ4 electron energy input for high and low solar flux years. *Journal of Geophysical Research*, *112*, A12301. https://doi.org/10.1029/2007JA012323
Lee, Y.-S., & Shepherd, G. G. (2010). Summer high-latitude mesospheric observations of supersonic bursts and O(1S) emission rate with the UARS WINDII instrument and the association with sprites, meteors, and lightning. *Journal of Geophysical Research*, *115*, A00E26. https://doi.org/10.1029/2009JA014731
Lehtinen, M. S., & Huuskonen, A. (1996). Grand unified incoherent scatter design and analysis package. *Journal of Atmospheric and Terrestrial Physics*, *58*, 435–452.
Li, W., Thorne, R. M., Angelopoulos, V., Bortnik, J., Cully, C. M., Ni, B., et al. (2009). Global distribution of whistler-mode chorus waves observed on the THEMIS spacecraft. *Geophysical Research Letters*, *36*, L09104. https://doi.org/10.1029/2009GL037595
Lubken, F.-J., Lehmacher, G., Blix, T., Hoppe, U.-P., Thrane, E., Cho, J., & Swartz, W. (1993). First in-situ observations of neutral and plasma density fluctuations within a PMSE layer. *Geophysical Research Letters*, *20*, 2311–2314. https://doi.org/10.1029/93GL00851
Manninen, J., Kleimenova, N. G., Kozyreva, O. V., & Ranta, A. (2002). High-latitude geomagnetic pulsation response to the passage of the front edge of the interplanetary magnetic cloud of January 10, 1997. *Journal of Atmospheric and Solar: Terrestrial Physics*, *64*, 1855–1864.
Meredith, N. P., Horne, R. B., & Anderson, R. R. (2001). Substorm dependence of chorus amplitudes: Implications for the acceleration of electrons to relativistic energies. *Journal of Geophysical Research*, *106*(A6), 13,165–13,178. https://doi.org/10.1029/2000JA900156
O'Brien, T. P., Lorentzen, K. R., Mann, I. R., Meredith, N. P., Blake, J. B., Fennell, J. F., et al. (2003). Energization of relativistic electrons in the presence of ULF power and MeV microbursts: Evidence for dual ULF and VLF acceleration. *Journal of Geophysical Research*, *108*(A8), 1329. https://doi.org/10.1029/2002JA009784
Poppoff, I. G., & Whitten, R. C. (1962). D-region ionization by solar X rays. *Journal of Geophysical Research*, *67*(7), 2986–2988. https://doi.org/10.1029/JZ067i007p02986
Rapp, M., & Lübken, F.-J. (2003). On the nature of PMSE: Electron diffusion in the vicinity of charged particles revisited. *Journal of Geophysical Research*, *108*(D8), 8437. https://doi.org/10.1029/2002JD002857
Rapp, M., & Lübken, F.-J. (2004). Polar mesosphere summer echoes (PMSE): Review of observations and current understanding. *Atmospheric Chemistry and Physics*, *4*, 2601–2633.
Safargaleev, V., Kozlovsky, A., Honary, F., Voronin, A., & Turunen, T. (2010). Geomagnetic disturbances on ground associated with particle precipitation during SC. *Annales Geophysique*, *28*, 247–265.
Saito, T. (1978). Long-period irregular magnetic pulsation, Pi3. *Space Science Reviews*, *21*, 427–467.
Sinnhuber, M., Nieder, H., & Wieters, N. (2012). Energetic particle precipitation and the chemistry of the mesosphere/lower thermosphere. *Surveys in Geophysics*, *33*, 1281–1334. https://doi.org/10.1007/s10712-012-9201-3
Strelnikova, I., & Rapp, M. (2011). Majority of PMSE spectral widths at UHF and VHF are compatible with a single scattering mechanism. *Journal of Atmospheric and Solar: Terrestrial Physics*, *73*, 2142–2152.
Takahashi, K., & Ukhorskiy, A. Y. (2007). Solar wind control of Pc5 pulsation power at geosynchronous orbit. *Journal of Geophysical Research*, *112*, A11205. https://doi.org/10.1029/2007JA012483
Turunen, T., Westman, A., Häggström, I., & Wannberg, G. (2002). High resolution general purpose D-layer experiment for EISCAT incoherent scatter radars using selected set of random codes. *Annales Geophysique*, *20*, 1469–1477. https://doi.org/10.5194/angeo-20-1469-2002
Varney, R. H., Kelley, M., Nicholls, M. C., Heinselman, C. J., & Collins, R. L. (2011). The electron density dependence of polar mesospheric summer echoes. *Journal of Atmospheric and Solar: Terrestrial Physics*, *73*, 2153–2165.
Velinov, P. (1968). On ionization in the ionospheric D-region by galactic and solar cosmic rays. *Journal of Atmospheric and Solar: Terrestrial Physics*, *30*(11), 1891–1905.
Waters, C. L., Takahashi, K., Lee, D.-H., & Anderson, B. J. (2002). Detection of ultralow-frequency cavity modes using spacecraft data. *Journal of Geophysical Research*, *107*(A10), 1284. https://doi.org/10.1029/2001JA000224
Williams, P. J. S., van Eyken, A. P., Hall, C., & Röttger, J. (1989). Modulations in the polar mesosphere summer echoes and associated atmospheric gravity waves. *Geophysical Research Letters*, *16*, 1944–8007. https://doi.org/10.1029/GL016i012p01437
Wilson, C. R. (1969). Auroral infrasonic waves. *Journal of Geophysical Research*, *74*(7), 1812–1836. https://doi.org/10.1029/JA074i007p01812
Yi, W., Reid, I. M., Xue, X., Younger, J. P., Murphy, D. J., Chen, T., & Dou, X. (2017). Response of neutral mesospheric density to geomagnetic forcing. *Geophysical Research Letters*, *44*, 8647–8655. https://doi.org/10.1002/2017GL074813
Yi, W., Reid, I. M., Xue, X., Younger, J. P., Spargo, A. J., Murphy, D. J., et al. (2017). First observation of mesosphere response to the solar wind high-speed streams. *Journal of Geophysical Research: Space Physics*, *122*, 9080–9088. https://doi.org/10.1002/2017JA024446
Zeller, O., & Bremer, J. (2009). The influence of geomagnetic activity on mesospheric summer echoes in middle and polar latitudes. *Annales Geophysique*, *27*, 831–837.

Zhou, X.-Y., & Tsurutani, B. T. (1999). Rapid intensification and propagation of the dayside aurora: Large scale interplanetary pressure pulses (fast shocks). *Geophysical Research Letters*, *26*, 1097–1100. https://doi.org/10.1029/1999GL900173

Zolotukhina, N. A., Mager, P. N., & Klimushkin, D. Y. (2008). Pc5 waves generated by substorm injection: A case study. *Annales Geophysique*, *26*, 2053–2059.